Vortices in quantum droplets of heteronuclear Bose mixtures

Matteo Caldara [1,2] and Francesco Ancilotto [3,4]

[1]*Dipartimento di Fisica e Astronomia "Galileo Galilei," Università di Padova, via Marzolo 8, 35122 Padova, Italy*

[2]*International School for Advanced Studies (SISSA), Via Bonomea 265, 34136 Trieste, Italy*

[3]*Dipartimento di Fisica e Astronomia "Galileo Galilei" and CNISM, Università di Padova, via Marzolo 8, 35122 Padova, Italy*

[4]*CNR-IOM Democritos, via Bonomea 265, 34136 Trieste, Italy*

(Received 4 February 2022; revised 13 April 2022; accepted 21 June 2022; published 30 June 2022)

We have theoretically investigated the structure of spinning self-bound droplets made of a ^{41}K - ^{87}Rb Bose mixture by solving the Gross-Pitaevskii equation including beyond-mean-field correction in the Lee-Huang-Yang form. The structure and energetics of vortex formation in the self-bound mixture have been elucidated, showing that the formation of linear vortices in the heavier species is energetically favored over other configurations. A fake (partially filled) core develops as a consequence in the other species, resulting in a hole which might be imaged in experiments. We computed the minimal size of ^{41}K $-$ ^{87}Rb droplets which can host stable vortex lines in their interior, which is important information for experiments aimed at the observation of vortices in such systems. The different role of quantized vortices and capillary waves, which are the two ways angular momentum can be stored in a swirling superfluid, is addressed in detail by computing the relation between angular momentum and rotational frequency. The results show intriguing similarities with the case of a prototypical superfluid, i.e., ^{4}He droplets when set into rotation. A two-branches curve in the stability diagram, qualitatively similar to the one expected for classical (incompressible and viscous) rotating liquid droplets, is obtained when vortices are present in the droplets, while prolate (i.e., nonaxisymmetric) shapes are only permitted in vortex-free droplets.

DOI: 10.1103/PhysRevA.105.063328

I. INTRODUCTION

A new quantum state of matter has been predicted [1] and shortly thereafter experimentally observed [2–5] in ultracold atomic gases made of a binary mixture of Bose atoms, where the competition between interspecies attractive interactions and quantum fluctuations, which act as a repulsive interaction, may result in the formation of self-bound, ultradilute liquid droplets, with typical densities being about eight orders of magnitude lower than those of the prototypical quantum fluid, i.e., liquid helium, at room pressure. Self-bound quantum liquid droplets have been predicted and observed in dipolar Bose gases as well [6–9], with a similar stabilizing mechanism.

Heteronuclear quantum droplets (QD) in a bosonic mixture of ^{41}K and ^{87}Rb have been experimentally realized more recently [4], and also in the ^{23}Na - ^{87}Rb mixture [5]. At variance with the largely studied homonuclear ^{39}K - ^{39}K mixture of K atoms in two different hyperfine states, the ^{41}K and ^{87}Rb mixture is characterized by longer lifetimes, of the order of several tens of milliseconds, i.e., more than a factor 10 larger than those characterizing the ^{39}K mixtures [3]. The longer lifetime is mainly a consequence of the smaller densities of the two components that result from the stronger intraspecies interactions. It follows that the regime of interaction parameters for which self-bound droplets form is such that three-body losses are expected to be significantly reduced, at variance with the ^{39}K - ^{39}K mixture where much stronger three-body losses continuously drive the system out of equilibrium, eventually leading to the depletion of the droplet. Longer lifetimes offer the possibility of investigating the collective modes of the droplets, likely allowing the observation of droplet self-evaporation [10]. Moreover, this will also favor the realization of larger droplets, characterized by a flat-top density profile encompassing a "bulk" region with a nearly constant saturation density and a surface region whose width is determined by the surface tension [11]. The crossover from compressible (i.e., smaller droplets characterized by an "all-surface," Gaussian-like profile) to incompressible (i.e., flat-top) quantum droplets, which is driven by the number of atoms, has been recently addressed experimentally in ^{39}K - ^{39}K droplet collision experiments [12] and studied with numerical simulations [12,13]. However, a clean interpretation of the experimental results seems to be hampered by the major role played in the ^{39}K - ^{39}K mixture by three-body loss factor, which is necessary in order to explain the experimental data [12,13], but whose actual value is affected by large uncertainties. For this reason, the ^{41}K - ^{87}Rb mixture appears to be a better candidate for a clear determination of the crossover.

Vortices are quantized topological excitations of superfluids and have been extensively studied over the years both in superfluid ^{4}He [14,15] and in cold bosonic atoms [16–18]. Although they should also appear under suitable conditions in quantum droplets, no experimental evidence of their existence has been gathered so far. There exist, however, a number of

theoretical papers addressing vorticity in quantum droplets made of Bose-Bose mixtures, mainly for two-dimensional systems, which are briefly reviewed in the following.

While vortices in quantum droplets made of dipolar condensates are found to be always unstable [19,20], in binary Bose-Einstein condensates (BEC) described by the Gross-Pitaevskii (GP) equation augmented by the beyond-mean-field correction in the Lee-Huang-Yang (LHY) form, they are found instead to be stable excitations when specific conditions are fulfilled [21–23]. Ground-state and rotational properties of two-dimensional self-bound quantum droplets made of a binary mixture of BECs are studied in Ref. [24]. Several phases are found depending on the system parameters, including center-of-mass excitation, ghost vortices, and vortices with single and multiple quantizations. The metastability of clusters made of quantum droplets is considered in Ref. [21] for a binary BEC in two dimensions, leading to the formation of ring-shaped clusters, possibly hosting "supervortices." Angular momentum-carrying droplets made of species-symmetric rotating binary BEC confined in two dimensions [25] are found to be unstable in free space and decay into fragments. When stabilized in a weak harmonic trap, and after switching off the trap potential, the rotational ground state displays an array of few metastable singly quantized vortices, with significant distortions of the droplet shapes from the axisymmetric configurations. The effects of vorticity on the breathing modes of these droplets have been addressed in Ref. [26]. Two-dimensional droplets carrying vorticity are investigated in Ref. [27], where axisymmetric QDs with heterosymmetric and heteromultipole structures, i.e., with different vorticities in each component and/or different multipolarities (singly or doubly quantized) are studied. The stability of vortical QDs was also studied in Refs. [23,28].

To our knowledge, only two theoretical papers address vortical states in three-dimensional quantum droplets made of Bose mixtures. In the first [29], droplets made of a two-component superfluid Bose mixture under rotation are studied and stationary states in the form of vortex rings with embedded topological charges $m_1 = m_2 = 1$ and $m_1 = m_2 = 2$ of the two components are found for sizes larger than some critical values. Droplets with hidden vorticity, i.e., with topological charges $m_1 = -m_2 = 1$ in the two components, are found instead to be always unstable and split into fragments. Equal scattering lengths a of the contact interactions in both components are assumed in Ref. [29], as well as equal masses for the two species.

In Ref. [30], whose focus is mainly on the thermodynamics conditions that leads to the formation of self-bound states in binary Bose mixtures, two examples of vortical configurations in self-bound droplets are provided, i.e., a singly and a doubly quantized vortex line in the center of a three-dimensional droplet made of the heteronuclear ^{23}Na - ^{87}Rb bosonic mixture and of the homonuclear ^{39}K - ^{39}K mixture as well. A singly quantized vortex nucleated in both species is found to be stable and robust against quadrupolar deformation, while the doubly quantized vortex eventually decays into pairs of singly quantized vortices. In both cases, the velocity field associated to the angular momentum stored in the droplet results in surface capillary waves that are responsible for the droplet distortion into a prolate shape and in the apparent rotation of the droplet as a whole. The results of Ref. [30] represent a very preliminary and limited study of vorticity in three-dimensional quantum droplets.

A more detailed study is presented here, where we address the properties of spinning three-dimensional droplets made of the ^{41}K - ^{87}Rb Bose mixture. We compute several properties of vortices in such QDs and focus on the relations among angular momentum, shape, and vorticity of quantum droplets. We also compute the minimum size that a QD must have to host a stable vortex in its interior. These properties have been the subject of recent experimental and theoretical studies on the prototype superfluid Bosonic system, where spinning ^{4}He nanodroplets have been investigated in a series of experiments [31–37]. Given the similarities between quantum droplets made of Bose mixtures and liquid ^{4}He droplets, as clarified in the following, we give here a brief account of recent theoretical and experimental studies on spinning superfluid ^{4}He nanodroplets.

We first recall here (the following discussion is partly taken from Ref. [38]) that the macroscopic behavior of a superfluid at zero temperature is described by the equations of irrotational hydrodynamics, from which the moment of inertia along the z axis can be calculated as [17,39] $\Theta_{\rm irr} = \varepsilon^2\,\Theta_{\rm rig}$, where

$$\varepsilon = \frac{\langle y^2 - x^2\rangle}{\langle y^2 + x^2\rangle} \tag{1}$$

$\Theta_{\rm rig} = Nm\langle x^2 + y^2\rangle$ is the rigid-body moment of inertia, N is the number of atoms in the droplet, and m is the atomic mass, showing that in a superfluid the value of the moment of inertia is smaller than the value for a rigid-body system. In particular, the above relation shows that for axisymmetric (i.e., oblate) systems, where $\langle x^2\rangle = \langle y^2\rangle$, the angular momentum of the superfluid along the z axis vanishes, $\langle \hat{L}_z\rangle = \Theta_{\rm irr}\,\omega = 0$, for any value of the rotational frequency. Therefore, oblate samples of a superfluid cannot spin, whereas prolate (non-axisymmetric) configurations can, and the resulting angular momentum $L_{\rm cap} = \Theta_{\rm irr}\,\omega$ is associated with the presence of capillary waves (see, for instance, Ref. [40]). Quantized vortex lines represent the other well-known mechanism with which angular momentum can be stored in spinning superfluids. In general, capillary waves and vortices may coexist in spinning droplets, as shown by experiments and theory for the ^{4}He case [37,38]. In the experiments [31–37] where ^{4}He liquid droplets may acquire angular momentum during the passage of the fluid through the nozzle of the molecular beam apparatus and where they were able to reconstruct images of the rotating ^{4}He droplets, *oblate* droplets were observed, which should be forbidden on quantum mechanical grounds. Thus, the only possible explanation for such experimental observation is that these drops must contain quantized vortices which can store most of the angular momentum of the droplet.

One striking outcome of these experiments was the finding that spinning superfluid ^{4}He droplets show unexpected similarities with the behavior of *classical* incompressible viscous droplets, only subject to surface tension and centrifugal forces [41–44]. It is precisely the presence of vortices in the droplet interior that confers on the spinning droplet the appearance and the properties of a rotating, classical viscous droplet, as also shown by density functional calculations [45,46]. A

well-known example of this apparently classical behavior of a rotating superfluid is the macroscopic meniscus that develops, at the liquid-vapor interface, in a rotating bucket filled with superfluid ^{4}He above the critical angular velocity required for vortex nucleation [14,47,48]. Similarities with the classical behavior of rotating viscous droplets are also displayed, as shown in the following, by rotating QDs.

II. METHOD

The Gross-Pitaevskii energy functional for a Bose-Bose mixture, including the Lee-Huang-Yang correction accounting for quantum fluctuations beyond mean field, reads [1,30]

$$E = \sum_{i=1}^{2} \int d\mathbf{r} \left[\frac{\hbar^2}{2m_i} |\nabla \psi_i(\mathbf{r})|^2 + V_i(\mathbf{r}) \rho_i(\mathbf{r}) \right] + \frac{1}{2} \sum_{i,j=1}^{2} g_{ij} \int d\mathbf{r}\, \rho_i(\mathbf{r}) \rho_j(\mathbf{r}) + \int d\mathbf{r}\, \mathcal{E}_{\rm LHY}(\rho_1(\mathbf{r}), \rho_2(\mathbf{r})) \tag{2}$$

where $V_i(\mathbf{r})$ and $\rho_i(\mathbf{r}) = |\psi_i(\mathbf{r})|^2$ represent the external potential and the (number) density of each component ($i = 1$ for ^{41}K, $i = 2$ for ^{87}Rb). The coupling constants are $g_{11} = 4\pi a_{11}\hbar^2/m_1$, $g_{22} = 4\pi a_{22}\hbar^2/m_2$, and $g_{12} = g_{21} = 2\pi a_{12}\hbar^2/m_r$, where $m_r = m_1 m_2/(m_1 + m_2)$ is the reduced mass. The intraspecies s-wave scattering lengths a_{11} and a_{22} are both positive, while the interspecies one, a_{12}, is negative. The scattering parameters describing the intraspecies repulsion are fixed and their values are equal to $a_{11} = 65\, a_0$ [49] and $a_{22} = 100.4\, a_0$ [50]. Notice that a slightly different value for the K-K scattering length, $a_{11} = 62\, a_0$, has been used more recently [10].

The total number of bosons is $N = N_1 + N_2$. The number densities ρ_1, ρ_2 are normalized such that $\int_V \rho_1(\mathbf{r})\, d\mathbf{r} = N_1$ and $\int_V \rho_2(\mathbf{r})\, d\mathbf{r} = N_2$.

The LHY correction is [1,30]

$$\mathcal{E}_{\rm LHY} = \frac{8}{15\pi^2} \left(\frac{m_1}{\hbar^2} \right)^{3/2} (g_{11}\rho_1)^{5/2} f\left(\frac{m_2}{m_1}, \frac{g_{12}^2}{g_{11} g_{22}}, \frac{g_{22}\, \rho_2}{g_{11}\, \rho_1} \right) \equiv \mathcal{C} (g_{11}\rho_1)^{5/2} f(z, u, x). \tag{3}$$

Here $f(z, u, x) > 0$ is a dimensionless function, whose explicit expression for $z \neq 1$ and $u = 1$ can be found in Ref. [30]. Following Ref. [1], we consider this function at the mean-field collapse $u = 1$, i.e., $f(z, 1, x)$. We note that the actual expression for f can be fitted very accurately with the same functional form of the homonuclear case ($m_1 = m_2$) [51]

$$f(z, 1, x) \simeq (1 + z^{\alpha} x)^{\beta}, \tag{4}$$

where α and β are fitting parameters. For the K-Rb mixture ($z = 87/41$), we found $\alpha = 0.586$ and $\beta = 2.506$, which are very close to the values $\alpha = 3/5$ and $\beta = 5/2$ proposed in Ref. [51] under the assumption that α and β are independent of the mass ratio z.

Minimization of the action associated to Eq. (2) leads to the following Euler-Lagrange (EL) equations (*generalized* GP equations)

$$i\hbar \frac{\partial \psi_i}{\partial t} = \left[-\frac{\hbar^2}{2m_i} \nabla^2 + V_i + \mu_i(\rho_1, \rho_2) \right] \psi_i \equiv \mathcal{H}_i \psi_i, \tag{5}$$

where

$$\mu_i = g_{ii}\rho_i + g_{ij}\rho_j + \frac{\partial \mathcal{E}_{\rm LHY}}{\partial \rho_i} \quad (j \neq i) \tag{6}$$

and

$$\frac{\partial \mathcal{E}_{\rm LHY}}{\partial \rho_1} = \mathcal{C} g_{11} (g_{11}\rho_1)^{3/2} \left(\frac{5}{2} f - x \frac{\partial f}{\partial x} \right), \tag{7}$$

$$\frac{\partial \mathcal{E}_{\rm LHY}}{\partial \rho_2} = \mathcal{C} g_{22} (g_{11}\rho_1)^{3/2} \frac{\partial f}{\partial x}, \tag{8}$$

where $\mathcal{C}$ is defined in Eq. (3). The above equations are solved by mapping the system (densities, wave functions, differential operators, etc.) on discrete equally spaced Cartesian grids. The differential operators are represented by a 13-point discretization. We solve the above equations by propagating the wave functions ψ_i in imaginary time, if stationary states are sought, or by propagating them in real time to simulate the dynamics of the system starting from specified initial states. The time-dependent equations have been solved by using the Hamming's predictor-modifier-corrector method, initiated by a fourth-order Runge-Kutta-Gill algorithm [52]. The spatial mesh spacing and time step are chosen such that during the time evolution excellent conservation of the total energy of the system is guaranteed.

In order to deposit angular momentum in the droplet, we have used an "imprinting" procedure [52] by starting the imaginary time minimization from a flexible guess for the effective wave function $\psi_0(\mathbf{r})$ for a given species, namely a superposition of a quadrupolar capillary wave and n_v vortex lines parallel to the z axis,

$$\psi_0(\mathbf{r}) = \rho_0^{1/2}(\mathbf{r})\, e^{i\alpha xy} \prod_{j=1}^{n_v} \frac{(x - x_j) + i(y - y_j)}{\sqrt{(x - x_j)^2 + (y - y_j)^2}}. \tag{9}$$

Here, $\rho_0(\mathbf{r})$ is an arbitrary, vortex-free droplet density, the complex phase $e^{i\alpha xy}$ imprints a capillary wave with quadrupolar symmetry around the z axis, and the product term imprints a vortex array made of n_v linear vortices [52], where (x_j, y_j) is the initial position of the jth vortex core. The initial value of α and the vortex core positions are guessed, and ψ_0 is optimized by iteratively solving Eqs. (5): During the minimization process both the vortex core structure and positions, together with the droplet shape, change to provide at convergence the lowest total energy configuration.

To study spinning droplets, it is convenient to work in the fixed-droplet frame of reference (corotating frame at angular velocity ω); i.e., we consider the functional

$$E' = E - \omega \langle \hat{L}_z \rangle, \tag{10}$$

where $\hat{L}_z$ is the total angular momentum operator in the z direction; one looks for solutions of the EL equation resulting

from the functional variation of E'

$$\{\mathcal{H}_i - \omega\hat{L}_z\}\,\psi_i(\mathbf{r}) = \mu_i\,\psi_i(\mathbf{r}), \tag{11}$$

where $\mathcal{H}_i$ ($i = 1, 2$) are defined in Eq. (5).

Two alternative strategies can be employed to solve the previous equations; i.e., one can either (i) fix ω and find the associated stationary configuration, which will be characterized by some value of the angular momentum $L = \langle\hat{L}_z\rangle$ depending upon the chosen value of ω, or (ii) solve it by imposing a given value for L and iteratively find the associated value of ω. Classically, the fixed ω calculations correspond to forced rotation conditions ("driven drops"), while the fixed L calculations correspond to torque-free drops with an initially prescribed rotation ("isolated drops"). Both methods will be used here, as it turns out that stable prolate configurations can only be found by using method (ii), i.e., fixing the value of L from the start [41–43]. At variance, stable oblate configurations can be found either by fixing ω or L [41].

Working at fixed angular momentum requires to adjust iteratively the value of ω: There are efficient ways of doing this, such as the augmented Lagrangian method [53] (used here), which consists in evolving the system using the Hamiltonians

$$\mathcal{H}_i' = \mathcal{H}_i - [\omega - \mu_L(\langle\hat{L}_z\rangle - L)]\hat{L}_z \tag{12}$$

and updating at each time step the angular velocity according to

$$\omega_{\text{new}} = \omega_{\text{old}} - \mu_L(\langle\hat{L}_z\rangle - L), \tag{13}$$

where μ_L is a positive constant controlling the rate of convergence toward a state with the imposed value L of the angular momentum.

III. RESULTS

A. Surface tension and healing length

As discussed in Sec. III E, results for rotating liquid droplets can be better interpreted in terms of rescaled units of the rotational frequency and angular momentum, whose definitions require the knowledge of the surface tension of the system. Moreover, the widths of the vortex cores in the quantum droplets are related to the healing lengths of the mixture. For this reason, we report in the following the calculated values of both these quantities for the ^{41}K - ^{87}Rb mixture. From now on, we will refer to ^{41}K as the first species and to ^{87}Rb as the second species.

While all the calculations described in the present work are obtained by solving the two coupled Eqs. (5), as far as the surface tension and the healing length are concerned, we use (as often done in the literature; see, for instance, Ref. [2]) a simpler single-component density functional, as briefly described in the following.

The equilibrium density of a droplet at $T = 0$ is obtained by requiring the vanishing of the total pressure, which yields the condition [1]

$$\frac{\rho_2}{\rho_1} = \sqrt{\frac{g_{11}}{g_{22}}}. \tag{14}$$

If one assumes that this optimal composition is realized everywhere in the system, the energy functional (3) becomes effectively single component, and can be written in terms of a single density only. By defining the following coefficients,

$$\alpha = \frac{1}{4}\left(\frac{\hbar^2}{2m_1} + \frac{\hbar^2}{2m_2}\sqrt{\frac{g_{11}}{g_{22}}}\right), \tag{15}$$

$$\beta = g_{11} + g_{12}\sqrt{\frac{g_{11}}{g_{22}}}, \tag{16}$$

$$\gamma = \frac{8}{15\pi^2}\left(\frac{m_1}{\hbar^2}\right)^{3/2} g_{11}^{5/2}\left[1 + \left(\frac{m_2}{m_1}\right)^{3/5}\sqrt{\frac{g_{22}}{g_{11}}}\right]^{5/2}, \tag{17}$$

the effective single-component energy density of the mixture, expressed for simplicity in terms of the density ρ_1 of the first species, reads

$$\mathcal{E} = \alpha\frac{(\nabla\rho_1)^2}{\rho_1} + \beta\rho_1^2 + \gamma\rho_1^{5/2} \tag{18}$$

so that $E = \int d\mathbf{r}\,\mathcal{E}$.

Self-bound quantum droplets are, by definition, systems with a finite surface tension. Remarkably, the surface tension for a planar interface separating a self-bound quantum liquid from vacuum can be estimated, without any prior knowledge of the density profile, by calculating the following integral [54],

$$\sigma = 2\int_0^{\rho_0} d\rho_1\,\sqrt{\alpha\left(\beta\rho_1 + \gamma\rho_1^{3/2} - \mu_0\right)}, \tag{19}$$

where $\mu_0 = \beta\rho + \gamma\rho^{3/2}$ is the chemical potential of a liquid system in equilibrium with the vacuum, evaluated at the equilibrium density $\rho = \rho_0$.

The surface tension of the binary mixture ^{41}K - ^{87}Rb has been computed for different values of the interspecies scattering length a_{12} in Ref. [11]. It turns out that relatively small changes in the interspecies interaction strength cause order-of-magnitude changes in the surface tension [11], which ranges from $\sigma \approx 10^2$ nK/μm^2 for $a_{12} = -80\,a_0$ to $\sigma \approx 10^5$ nK/μm^2 for $a_{12} = -100\,a_0$. We show for clarity in Fig. 1 the values of σ for the ^{41}K - ^{87}Rb mixture, as calculated in Ref. [11].

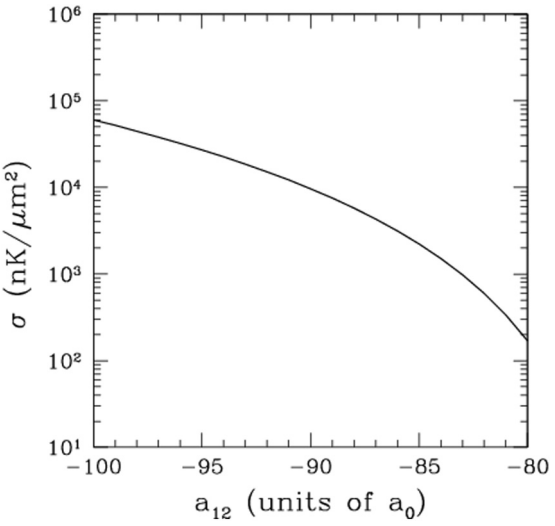

FIG. 1. Surface tension of the ^{41}K - ^{87}Rb quantum liquid as a function of the interspecies scattering length a_{12} (from Ref. [11]).

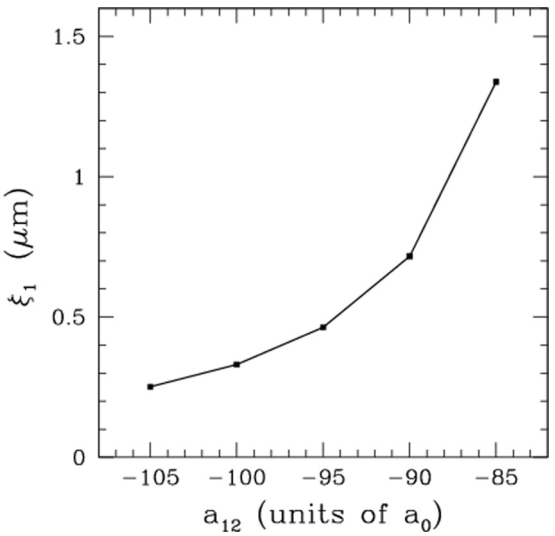

FIG. 2. Healing lengths of the ^{41}K - ^{87}Rb quantum liquid as a function of the interspecies scattering length a_{12}.

An explicit expression for the healing length of the self-bound ^{41}K - ^{87}Rb mixture can be obtained as the length scale where the kinetic energy of the system equals the chemical potential. In this way, one can derive the following expression for the healing length in the first species and second species, respectively:

$$\xi_1 = \left(- \frac{2\alpha}{2\beta\rho_1 + \frac{5}{2}\gamma\rho_1^{3/2}} \right)^{1/2}, \tag{20}$$

$$\xi_2 = \left(- \frac{2\alpha}{2\beta\sqrt{\frac{g_{22}}{g_{11}}}\rho_2 + \frac{5}{2}\gamma\left(\frac{g_{22}}{g_{11}}\right)^{3/4}\rho_2^{3/2}} \right)^{1/2}. \tag{21}$$

Notice that if the optimal ratio between the two densities is exactly realized, then $\xi_1 = \xi_2$. We plot in Fig. 2 the calculated healing length ξ_1 for different values of the interspecies scattering length a_{12}.

B. Vortices in the extended system

In order to achieve a better understanding of the intrinsic properties of vortices in the ^{41}K - ^{87}Rb mixture, we first studied, by solving the two-component system (5), isolated vortices in an *extended* ^{41}K - ^{87}Rb system for different values of the scattering length a_{12} in the range where the formation of self-bound liquid is expected: For this specific mixture, this occurs for $a_{12} < -75.4\,a_0$. With an extended system, we refer to a uniform mixture where the densities are constant inside the whole three-dimensional simulation domain, with a ratio given by Eq. (14). In this way, the calculated vortex core properties (as computed in the following) become independent on the droplet size, the extended system being equivalent to a droplet with an infinite radius.

The initial state is represented by Eq. (9), where we take $\alpha = 0$ and imprint just a single vortex in the center of the system (on the $x - y$ plane), with ρ_0 equal to the bulk density for the species hosting the vortex. The flow field of a linear vortex has a long-range character, $\sim 1/r$, r being the distance from the vortex axis (namely, the z axis). We have imposed, during the minimization, antiperiodic boundary conditions [55] in the $x - y$ plane in order to satisfy the condition of no flow across the boundary of the computational cell. Standard periodic boundary conditions are used, instead, along the z direction.

A measure of the vortex excitation energy per unit length of a linear vortex of length L is given by the integrated vortex kinetic energy [56,57], which can be defined as follows:

$$\epsilon_v(R) = \frac{1}{L}\left[E^v_{\rm kin}(R) - E^0_{\rm kin}(R)\right], \tag{22}$$

where $E^v_{\rm kin}$, $E^0_{\rm kin}$ are the kinetic energies within a cylinder of radius $R = \sqrt{x^2 + y^2}$ and length L (with and without a vortex line along the z axis, respectively) as a function of the distance R from the vortex line. $E^v_{\rm kin}(R)$ is given by the integral $\int_0^L dz 2\pi \int_0^R dR'\, R'\, \epsilon(R')$, where $\epsilon(R) = (\hbar^2/2m)|\nabla_R \psi_i|^2$, and $\nabla_R \equiv (\partial/\partial x, \partial/\partial y)$ (i is the index of the vortex-hosting component of the mixture). Similar expressions hold for $E^0_{\rm kin}(R)$.

We notice that the classical hydrodynamical counterpart of $\epsilon_v(R)$ for a vortex in an incompressible fluid of density ρ_0 and circulation κ is

$$\epsilon_v^{\rm hydro}(R) = \frac{\kappa^2}{4\pi} m\rho_0 \left[\ln\left(\frac{R}{d_v}\right) + \delta \right], \tag{23}$$

where d_v is the vortex core radius and δ depends on the model for the core ($\delta = 0$ for the hollow core model and $\delta = 1/4$ for a core in rigid rotation) [14]. The parameter δ in the previous equation can be absorbed in the logarithmic term; using the quantum value for the circulation, $\kappa = h/m$, $\epsilon_v^{\rm hydro}$ reads

$$\epsilon_v^{\rm hydro}(R) = \frac{\hbar^2}{m}\pi\rho_0 \ln\left(\frac{R}{\lambda}\right) \tag{24}$$

for a singly quantized vortex, where $\lambda = d_v e^{-\delta}$ is the core parameter.

We compute the lowest energy solution, for different values of the interspecies scattering length a_{12}, starting from the initial state given by Eq. (9), and then make a best-fit interpolation of the calculated vortex kinetic energy $\epsilon_v(R)$, as defined in Eq. (22), with the hydrodynamic approximation for the vortex excitation energy (the vortex being in the species i) given by Eq. (24), using ρ_0 and λ as fitting parameters. We will consider two cases: (i) both species embed a singly quantized vortex with a common core position and (ii) a singly quantized vortex is imprinted in one species only. Therefore in the first case the phase change around the core position is 2π when calculated separately for the two species, while in the second case the phase change is zero for the species which does not embed any vorticity.

We find that the hydrodynamic expression (24) accurately reproduces the calculated excitation energies far from the vortex line. By comparing the calculated kinetic energy with that predicted by Eq. (24), we computed the core parameter λ as a function of a_{12}. We found, with good accuracy, that $\lambda_i = 1.07\,\xi_i$ when both species host a singly quantized vortex. When a vortex is imprinted in the first species only, K, we find $\lambda_1 = 0.82\,\xi_1$, whereas we find $\lambda_2 = 0.53\,\xi_2$ for a vortex in the Rb species only. These ratios are independent on the chosen values for a_{12}.

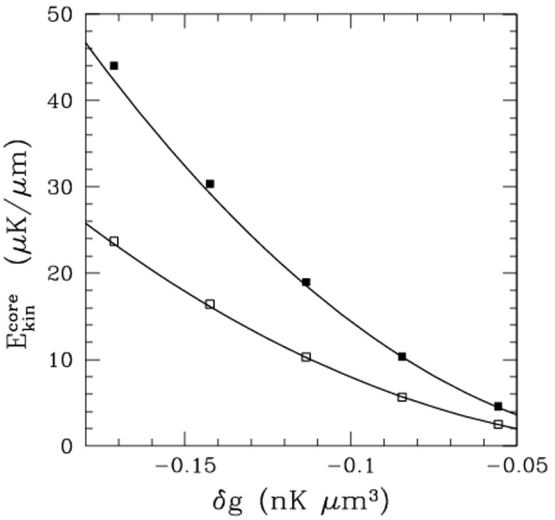

FIG. 3. Core energies for the two species as a function of the parameter δg. Filled squares: First species (K); open squares: Second species (Rb). The solid lines are obtained from Eq. (25).

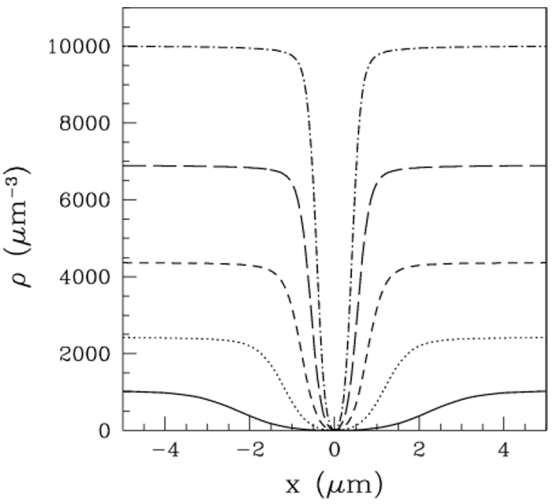

FIG. 4. Total density $\rho_1 + \rho_2$ along a line passing through the core of a vortex imprinted in both species, for different values of the interspecies scattering length a_{12}. From top to bottom: $a_{12} = -105,\ -100,\ -95,\ -90,\ -85\,a_0$.

As expected, the approximation breaks down at distances approaching the vortex core, as there the local density becomes very small. The radius R_c of the vortex core region is defined here as the distance from the center at which the modulus of the wave function is equal to half the value it takes far from the core region. From this, the vortex "core" energy, defined as $E^{\mathrm{core},i} = E_{\mathrm{kin},i}(R_c)$, is thus obtained. The calculated values are shown in Fig. 3 as a function of $\delta g = g_{12} + \sqrt{g_{11}g_{22}}$, for the case where a singly quantized vortex is embedded in each species.

We found that the core energies $E^{\mathrm{core},i}$ are well approximated by the expression (solid lines in Fig. 3)

$$\frac{E^{\mathrm{core},i}}{L} = \frac{\pi}{4}\frac{\hbar^2}{m_i}K_i\delta g^2, \tag{25}$$

where K_i are the coefficients relating the densities for the uniform system to δg^2, i.e.,

$$\rho_1 = \frac{25\pi}{1024}\frac{1}{a_{11}^3}\frac{f^{-2}(z,1,x)}{g_{11}g_{22}}\delta g^2 \equiv K_1\delta g^2 \tag{26}$$

and similarly for $\rho_2 = \sqrt{g_{11}/g_{22}}\,\rho_1$.

When a singly quantized vortex is imprinted in both species, the resulting density profile is shown in Fig. 4. As the scattering length becomes more negative, the vortex core shrinks. The core in the total density is empty since both species host a vortex line.

When the vortex is in the second, heavier species only (Rb), the profiles look like those in Fig. 5. Notice that the vortex core size is reduced with respect to the previous case, and moreover the core is partially filled by the first species, which hosts no vorticity. Similar profiles, characterized by a core that is partially filled with the species without vorticity, are found when the vortex is imprinted in the first species only (K).

We compare in Fig. 6 the vortex structure, close to the core region, for the two cases: (i) both species host a singly quantized vortex and (ii) only the second species hosts a singly quantized vortex (a similar behavior is found in the case where only the first species carries a vortex). In spite of the fact that only the second species carries vorticity, a deep depression develops also in the vortex-free species 1, mimicking a "fake" vortex core with a small residual density at the core position. A similar effect has been theoretically predicted for two-dimensional QDs made of binary homonuclear Bose mixture [27]. This is a consequence of the fact that the system tries to restore everywhere the optimal ratio between the densities [Eq. (14)], except very close to the core center. We observe that the amount of filling due to the species without vorticity decreases as a_{12} becomes less negative.

From the calculated density profiles, we computed the widths of the vortex cores, defined as the half-width at half-maximum of the density value far from the vortex position,

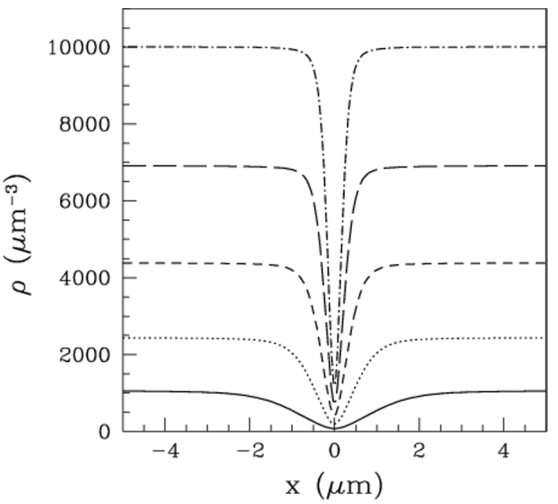

FIG. 5. Total density $\rho_1 + \rho_2$ along a line passing through the core when a single vortex is nucleated in the second species (Rb), for different values of the interspecies scattering length a_{12}. From top to bottom: $a_{12} = -105,\ -100,\ -95,\ -90,\ -85\,a_0$.

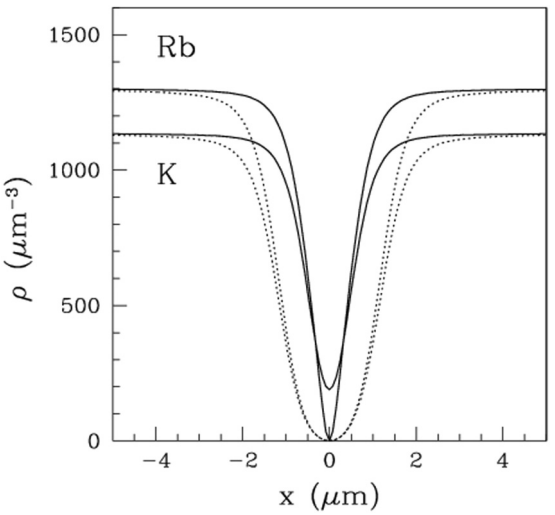

FIG. 6. Density profiles for each species, for the case $a_{12} = -90\,a_0$, for a vortex imprinted in both species (dotted lines), and a vortex imprinted only in the second one, Rb (solid lines): Notice that, in the latter case, the K density displays a partially filled core, as discussed in the text.

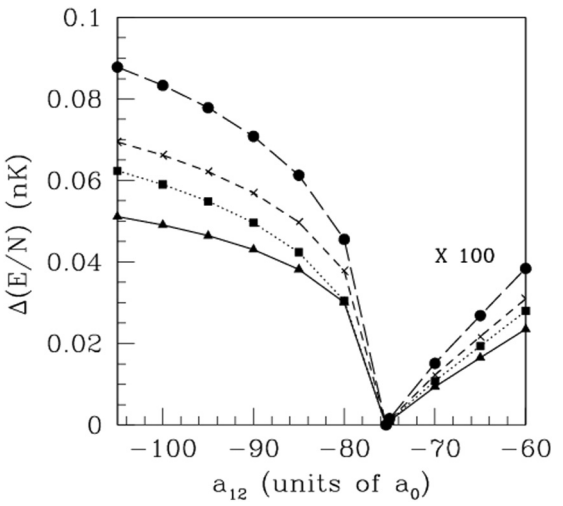

FIG. 8. Vortex formation energies (per pair) as a function of a_{12}. The value $a_{12} = -75.4\,a_0$ marks the crossover between the self-bound and the uniform (unbound) superfluid system. Values to the right of this point are multiplied by a factor 100 for clarity. Triangles, $2V_2$; squares, V_{1+2}; crosses, $V_1 + V_2$; dots, $2V_1$.

as a function of the scattering length a_{12}. We show the results in Fig. 7 for the cases where a vortex is imprinted either in one species or the other. It appears that the core widths in the lighter species, K, are twice as large as in Rb, and increase with a_{12}, as expected from the behavior of the healing length in Fig. 2. This could turn out to be a useful information to identify the vortex-hosting species in experiments, where the two species can be imaged separately.

In order to determine the most energetically favorable configuration of vortices in the mixture, we computed the energy cost to have (i) a vortex in both species and at the same position, (ii) two spatially separated vortices, both in the first species only, (iii) two spatially separated vortices, both in the second species only, and (iv) two spatially separated vortices, one in the first species and the other in the second species.

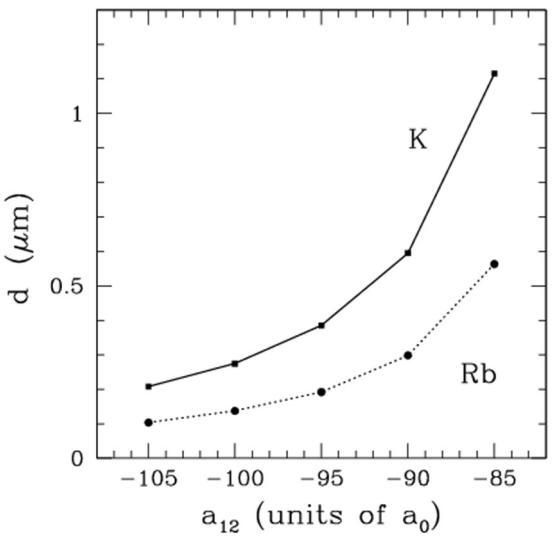

FIG. 7. Widths of the vortex cores, defined as the half-width at half-maximum of the density value far from the vortex, for the case of a vortex in the first species (K) only (black squares) and for a vortex in the second species (Rb) only (black dots).

The results, as a function of interspecies scattering length, are shown in Fig. 8, where we report the calculated energies per atom, $\Delta(E/N)$, where

$$\Delta(E/N)_{2V_i} = 2[(E/N)_{V_i} - (E/N)_0] \tag{27}$$

for two isolated vortices in the species $i = 1$ (K), $i = 2$ (Rb);

$$\Delta(E/N)_{V_{1+2}} = (E/N)_{V_{1+2}} - (E/N)_0 \tag{28}$$

for two vortices in the same position, one inside each species;

$$\Delta(E/N)_{V_1+V_2} = \sum_{i=1}^{2}(E/N)_{V_i} - 2(E/N)_0 \tag{29}$$

for two isolated vortices, one in the first species and one in the second species. Here $(E/N)_0$ is the energy for the vortex-free, uniform system.

We remark that in order to compute the energy of two isolated (i.e., spatially separated) vortices V_i and V_j $(i, j = 1, 2)$ we simply add the calculated energies [obtained by solving the GP Eq. (5)] of *single* vortex configurations V_i, so it is as if the two vortices were noninteracting with one another.

The results in Fig. 8 show that the most energetically favored configuration is the one with a vortex in the second species (Rb), whereas the least energetically favored is that with vortices in the first species (K) only.

The fact that nucleating vortices in the heavier species are energetically favored could be explained by recalling that the vortex energy (24) is essentially proportional to the ratio ρ/m, which is lower for the Rb species.

The same energetic ordering, albeit with much smaller energies (which appear multiplied by a factor 100 in Fig. 8 for clarity) persists also for the unbound superfluid mixture, i.e., for $|a_{12}| < 75.4\,a_0$. Notice that, in this superfluid miscible

regime, the overall interaction between atoms is repulsive and the LHY quantum correction provides only a subleading contribution with respect to the mean-field term that is described by the parameter $\delta g > 0$. As a result, vortex cores in the superfluid mixture have a larger extension with respect to the droplet case: The healing lengths in Eqs. (20) and (21) reduce to the standard expression for a single-component BEC, $\xi \propto (\delta g\, \rho)^{-1/2}$.

The results just presented for the *extended* system are representative to a large extent of the properties of vortices in droplets. Although in principle finite-size effects cannot be neglected in droplets, the minimal size of droplets hosting stable vortex lines, as shown in the following, is relatively large: For such droplets, the equilibrium density profile is flat-top, i.e., almost constant inside the bulk region and rapidly vanishing at the liquid-vacuum interface, and vortex cores are well contained within the bulk constant density region. As a result, we do not expect much differences with respect to the case of the extended system.

C. Nucleation of vortices from dynamical simulations

A possible way of producing in experiments QDs hosting vorticity could be to first nucleate vortices in a superfluid, unbound mixture (i.e., with a_{12} greater than the critical value for the stabilization of self-bound droplets) subject to harmonic confinement by, e.g., stirring the condensate with a laser beam or by using a rotating, slightly ellipsoidal radial trap. Then the scattering length a_{12} should be quenched to a more negative value, where the formation of a (much denser) QD is expected, and the harmonic confinement released at the same time. If the size of the droplet is large enough to accommodate one or more vortices, the final configuration would likely be a vortex-hosting QD.

Although such process could be simulated by performing time-dependent numerical simulations based on the extended GP equation described in Sec. II, it implies a huge computational cost in the present settings, due to the very large size of the droplets needed in order to host few stable vortices and due to the fine mesh in real space required to accurately represent the wave functions, especially in the vortex core regions. Therefore, we consider a ^{41}K-^{87}Rb mixture in a rotating cylindrical trap (described in the following) aligned with the rotational axis. We use periodic boundary conditions along the z direction, where the densities of the two species are constant (the system is translationally invariant along this direction). In this way, we reduce the calculations to an effectively two-dimensional system. Calculations are performed in the corotating frame, using Eq. (11) and fixed angular velocity.

We will only address a simplified version of the vortex nucleation process here, i.e., the dynamical nucleation of vortices in a rotating, trapped mixture in the superfluid, unbound phase (we notice that the stability of vortex states in a superfluid binary mixture in two dimensions has been studied in Ref. [58]). This will allow us to verify the above prediction that nucleation of singly quantized vortices in the Rb phase only will most likely occur. A more systematic study of the full process (i.e., the vortex nucleation in the rotating superfluid phase, followed by a quench of the interspecies scattering length into the self-bound regime, with the likely formation of vortex-carrying quantum droplets) will be the subject of a future study.

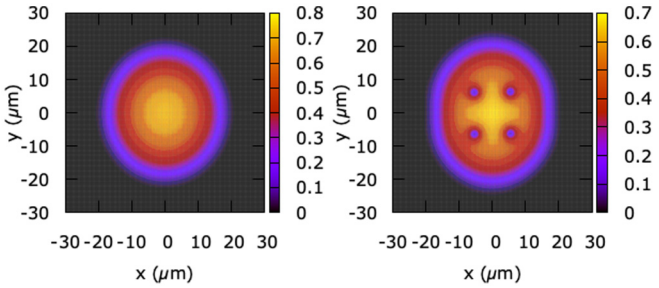

FIG. 9. 2D total density profiles on the xy plane of the SF cylinder. On the left, the equilibrium density profile at rest is shown: The deformation is due to the anisotropic harmonic potential. The right part of the figure shows the stationary configuration in the corotating frame with angular frequency ω, with four vortices nucleated in the second species (Rb). Lengths are expressed in μm, and densities are expressed in units of $10^2\ \mu\text{m}^{-3}$.

The interspecies scattering length is set to $a_{12} = -70\, a_0$ so that the system is just inside the miscible regime with $\delta g > 0$. Since the system is in the gaseous phase, an additional harmonic confining potential is necessary in order to stabilize it. The number of atoms for each species is $N_1 = 10^6$ and $N_2 = 1.1765 \times 10^6$: Notice that since the available volume is the same for both species, the atom numbers satisfy the optimal ratio in Eq. (14), $N_1/N_2 = \rho_1/\rho_2 = \sqrt{g_{22}/g_{11}}$. We use different trapping potentials acting on each species, through an additional term in the energy functional (2):

$$\mathcal{E}_{ho}[\rho_1, \rho_2] = \sum_{i=1}^{2} \frac{1}{2} m_i \left(\omega_{i,x}^2 x^2 + \omega_{i,y}^2 y^2\right) \rho_i(\mathbf{r}). \tag{30}$$

We choose here the trapping frequencies in such a way that the two species experience the same force constant along each direction, i.e., $m_1\omega_{1,\alpha}^2 = m_2\omega_{2,\alpha}^2$ $(\alpha = x, y)$ We also introduce a slight anisotropy in the trapping potential, $\omega_{1,x}/\omega_{1,y} = \omega_{2,x}/\omega_{2,y} = 1.1$, which favors the nucleation of vortices as the trap is rotated. The values used are $(\omega_{1,x}, \omega_{1,y}) = 2\pi \times (6.50, 5.91)\,\text{Hz}$ and $(\omega_{2,x}, \omega_{2,y}) = 2\pi \times (4.46, 4.06)\,\text{Hz}$. As for the rotational frequency in the corotating frame [see Eq. (10)] we use the value $\omega = 2\pi \times 3.1\,\text{Hz}$. The chosen value for ω must be higher than the critical value necessary to nucleate a single vortex line, which is of the order of $\omega_c = \frac{\hbar}{mR^2} \ln(\frac{R}{\lambda}) \sim 2\pi \times 0.9\,\text{Hz}$, where R is the average condensate radius in the $x - y$ plane and λ is the vortex core parameter.

The initial configuration of the imaginary-time dynamics is shown in the left panel of Fig. 9, which represents the ground-state configuration in the (stationary) elliptical trap.

The outcome of the imaginary-time dynamics is the spontaneous nucleation of four vortex lines in the second species (Rb), which enter the cylinder from the lateral surface and then move inside the bulk region until they reach a stationary position. In the final configuration, that is shown in the right panel of Fig. 9, these vortex lines are located at the same distance from the rotational axis. Angular momentum

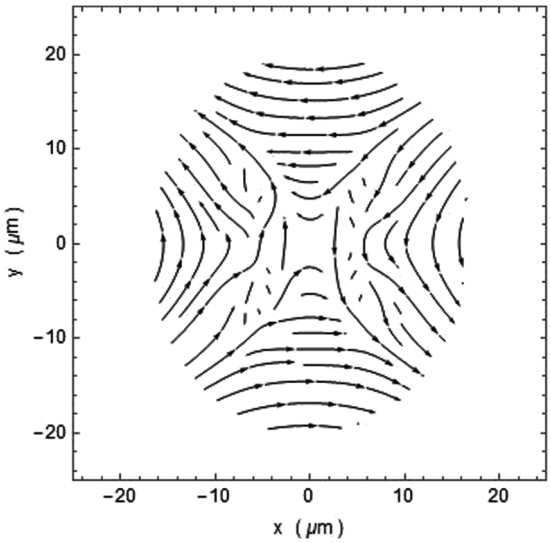

FIG. 10. Superfluid flow for the first species (K), shown with streamlines in the xy plane orthogonal to the rotation axis, for the rotating configuration shown in the right part of Fig. 9.

is stored in the first species (K) only through the quadrupolar deformation favored by the elliptical trap. We remark that the configurations shown in the figure are stationary in the corotating frame; as a consequence, they would be seen in the laboratory frame as if they were rotating with the angular frequency ω. This is indeed what we observed after performing a real-time dynamics with $\omega = 0$ starting from the configuration shown in the right panel of Fig. 9.

Streamlines of the superfluid flow are shown in Figs. 10 and 11, illustrating the irrotational velocity fields in each component. Streamlines allow to infer by visual inspection the coexistence of vortices and surface capillary waves, as their velocity fields are very different. The streamlines associated

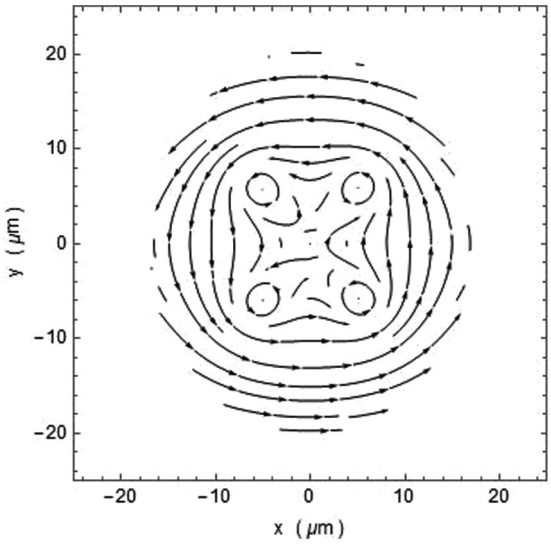

FIG. 11. Superfluid flow for the second species (Rb), shown with streamlines in the xy plane orthogonal to the rotation axis, for the rotating configuration shown in the right part of Fig. 9.

to vortices wrap around their cores, as in Fig. 11, whereas those associated to capillary waves end abruptly at the surface of the superfluid [37,59,60], as in Fig. 10: In the laboratory frame, this results in the rotation of the cloud as a whole, with angular frequency ω.

D. Critical droplet sizes for vortex stability

Not all values of $N = N_1 + N_2$ are allowed in a self-bound droplet for a given a_{12} because small droplets, made with a total number of atoms below some critical value N_c, become unstable when the kinetic energy dominates over the interaction energy, eventually causing the evaporation of the droplet itself. The critical size N_c for quantum droplets has been calculated for the ^{41}K-^{87}Rb mixture in Ref. [11]. In the presence of vortices, however, the critical size is expected to be larger, since the droplet must accommodate the vortex structure and the associated velocity field. We have estimated such critical size by computing a vortex-hosting droplet structure and check its stability during the evolution in time. We have studied first the case of two singly quantized vortices in a ^{41}K-^{87}Rb quantum droplet, one in each species: For a fixed value of a_{12} and a given total number of particles $N = N_1 + N_2$ (with $N_1/N_2 = \sqrt{g_{22}/g_{11}}$), one vortex line for each species was imprinted in the droplet center, aligned with the z direction, and the system was let to evolve in imaginary time in order to find the lowest energy stationary state. In this case, three possible outcomes of the minimization in the corotating frame are found: (i) *Unstable* regime: During the evolution in imaginary time the vortex core is gradually expelled from the droplet, which eventually recovers the lowest energy structure of a stable, vortex-free one. (ii) *Metastable* regime: During the evolution in imaginary time the system apparently converges toward a stable configuration with the vortex in the center of the droplet. However, starting a real-time dynamics from this state the system slowly (in a time of the order of 5 ms) expels the vortex and the droplet again recovers a stable, vortex-free structure. (iii) *Stable* regime: The system converges toward a stable configuration with the vortex cores aligned along the z direction and in the center of the droplet. These configurations are found to be robust against real-time evolution initiated from this converged stationary state.

In the case of the most energetically favored configuration, i.e., one vortex in the second species only, we find that there is not a metastable region: The vortices are either unstable and are eventually expelled from the droplet, or they stabilize inside the droplet. The critical line separating stable from unstable vortices is the dotted one shown in Fig. 12, compared with the similar line for the double-vortex case (solid line in the figure). As shown in Fig. 6, the core sizes in this configuration are smaller with respect to the previous one: This gives the possibility to smaller droplets to sustain a single vortex.

The results shown in Fig. 12 clearly show how the finite size of droplets strongly influence their capability to host stable vortex lines, especially as one approaches the superfluid-to-droplet transition. From the comparison with the critical size for vortex-free K-Rb droplets [11], it appears that the critical size for stability of a single vortex is much larger, of the order of 10^6 atoms. For comparison, at $a_{12} = -85\,a_0$

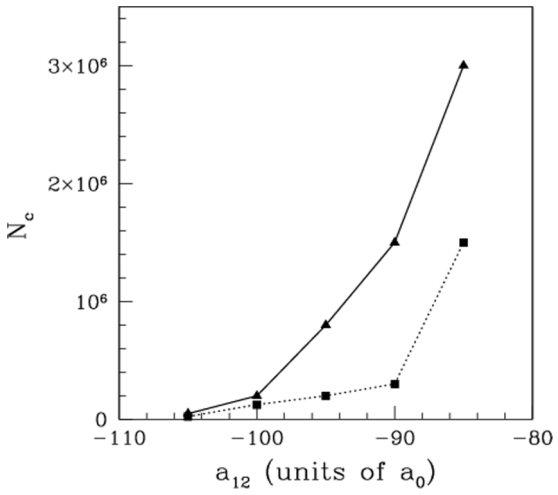

FIG. 12. Stability diagram showing the minimal size of droplets hosting a vortex. Solid line, one vortex in both species; dotted line, one vortex in the second species (Rb) only.

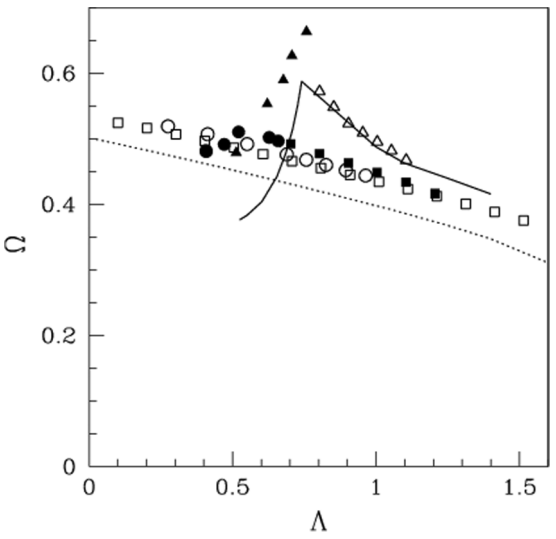

FIG. 13. Rescaled angular velocity Ω vs rescaled angular momentum Λ. Solid line, ^{4}He droplets [45] hosting vortices ($N = 1500$); dotted line, prolate vortex-free ^{4}He droplets [45] ($N = 1500$); black triangles, oblate 3-vortex droplets ($N = 9 \times 10^6$, $a_{12} = -95\,a_0$); open triangles, prolate 3-vortex droplets ($N = 1.5 \times 10^6$, $a_{12} = -105\,a_0$); open squares, prolate vortex-free droplets ($N = 10^5$, $a_{12} = -105\,a_0$); open circles, prolate vortex-free droplets ($N = 10^5$, $a_{12} = -90\,a_0$); black squares, prolate vortex-free droplets ($N = 1.5 \times 10^6$, $a_{12} = -105\,a_0$); black dots, prolate 2-vortex droplets ($N = 9 \times 10^6$, $a_{12} = -95\,a_0$).

the critical size for vortex-free droplets is $N \approx 20\,000$ [11]. We must notice that droplets of sizes above the lower critical line in Fig. 12 have not been experimentally realized so far for the K-Rb mixture.

E. Angular momentum and shapes in rotating K-Rb quantum droplets

The shapes of classical liquid droplets undergoing rigid-body rotation follow a universal stability diagram in terms of reduced angular momentum Λ and reduced angular velocity Ω (defined in the following). The configurations of rotating droplets lie on two possible branches in the Ω-Λ plane [33,42,43]:

(1) An ascending Ω(Λ) branch for lower values of Λ corresponding to oblate axisymmetric shapes: The higher Λ, the more squeezed is the droplet along the rotational axis.

(2) A descending Ω(Λ) branch for higher values of Λ describing prolate (i.e., nonaxisymmetric) shapes, such as ellipsoids, capsules, and dumbbells: The higher Λ, the more elongated are such droplets along an axis perpendicular to the rotational axis.

The two branches meet at the point $\Lambda = 1.2$ where they form a cusp.

The analysis of superfluid ^{4}He droplets rotating solely through capillary waves shows the presence of an additional descending Ω(Λ) branch in the stability diagram [38,46] that is peculiar to superfluid: This branch is populated by prolate (i.e., nonaxisymmetric) droplets, since these are the only configurations that can store a finite amount of angular momentum in the form of capillary waves.

We will use here rescaled units, as usually done for classical liquid droplets, which allow us to compare our results for different droplet sizes and values of a_{12} and also to compare our results with the ones for ^{4}He rotating droplets, in spite of the orders-of-magnitude differences in surface tensions and densities. Such units, in the case of a binary mixture, are defined as

$$\Omega \equiv \sqrt{\frac{(m_1\rho_1 + m_2\rho_2)\,R^3}{8\,\sigma}}\,\omega, \tag{31}$$

$$\Lambda \equiv \frac{1}{\sqrt{8\sigma R^7 (m_1\rho_1 + m_2\rho_2)}}\,L_z, \tag{32}$$

where σ is the surface tension of the ^{41}K-^{87}Rb mixture, shown in Fig. 1, and R is the sharp radius of a (spherical) droplet with $N = N_1 + N_2$ atoms, defined such that $4\pi R^3(\rho_1 + \rho_2)/3 = N$.

We investigated different configurations of QDs hosting a finite amount of angular momentum, with and without vortices, although the fully three-dimensional geometry used here and the need of fine meshes in real space severely limit the maximum sizes and number of vortices that we can address. We consider here droplets hosting vortices only in the second component, i.e., Rb, which is the most stable vortex configuration as shown in Sec. III B.

The equilibrium shapes of the rotating droplets are strongly influenced by the way in which angular momentum is stored (i.e., via capillary waves and/or vortices). The vortex-free droplets are, as expected, on a single branch, which characterizes prolate shapes: The angular momentum in these droplets can only be stored in the form of capillary waves, as discussed in the introduction. The calculated points in the Ω-Λ plane corresponding to prolate, vortex-free droplets (open squares and open circles in Fig. 13) are very close to the curve found for prolate ^{4}He droplets [38], as shown in Fig. 13. This

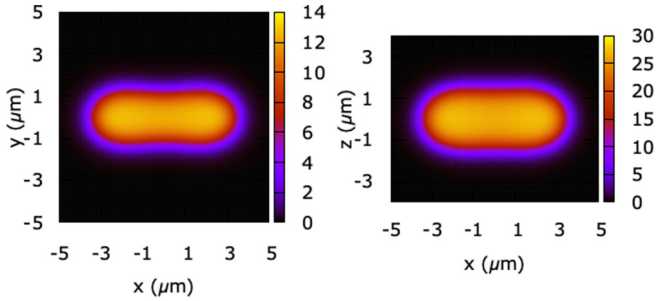

FIG. 14. Left: Total density ρ on the xy-symmetry plane perpendicular to the rotational axis for a prolate, vortex-free droplet with $N = 10^5$; right: Side view in the xz plane passing through the center of the droplet. Lengths are expressed in μm, and densities are expressed in units of 10^2 μm^{-3}.

(almost) universal behavior is a remarkable result given the very different natures of these two quantum liquids, whose surface tensions and densities differ by many orders of magnitude. An example of prolate vortex-free droplet (with $N = 10^5$ and for $a_{12} = -105\,a_0$) is shown in Fig. 14, corresponding to a value of the angular momentum $\Lambda = 1.1$. The two plots show the total density of the droplet in the xy-symmetry plane perpendicular to the rotation axis and in the xz plane containing the rotation axis.

When vortices are present in the droplet, however, the calculated points seem to follow a more "classical" behavior, characterized by a rising branch for oblate, vortex-hosting QDs, and a decreasing branch where prolate, vortex-hosting QDs lie instead (open and black triangles in Fig. 13). An example of oblate (axisymmetric) droplet (black triangles in the rising branch in Fig. 13) hosting three vortices in its interior (with $N = 1.6 \times 10^7$ and for $a_{12} = -90\,a_0$), corresponding to a value of the angular momentum $\Lambda = 0.7$, is shown in Fig. 15 by means of equal total density maps in the xy and xz symmetry planes, as in Fig. 14 (only the vortex whose core is contained in the xz plane passing through the center of the droplet appears in the right panel of Fig. 15).

Finally, an example of prolate droplet (open triangles in the decreasing branch in Fig. 13) hosting three aligned vortices in its interior (with $N = 1.5 \times 10^6$ and for $a_{12} = -90\,a_0$) corresponding to a value of the angular momentum $\Lambda = 0.9$, is

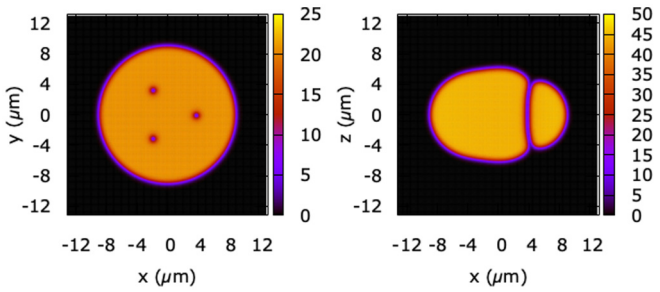

FIG. 15. Left: Total density ρ on the xy-symmetry plane perpendicular to the rotational axis for an oblate droplet hosting three vortices (only in Rb) with $N = 1.6 \times 10^7$; right: Side view in the xz plane passing through the center of the droplet. Lengths are expressed in μm, and densities are expressed in units of 10^2 μm^{-3}.

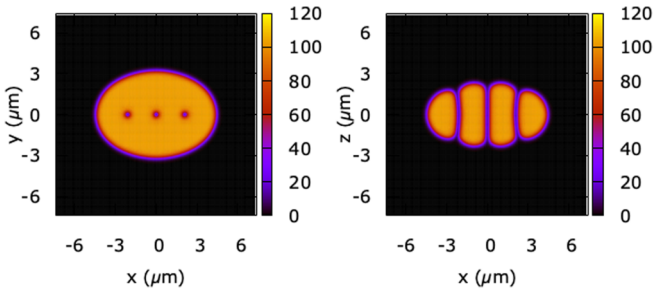

FIG. 16. Left: Total density ρ on the xy-symmetry plane perpendicular to the rotational axis for a prolate droplet hosting three vortices (only in Rb) with $N = 1.5 \times 10^6$; right: Side view in the xz plane passing through the center of the droplet. Lengths are expressed in μm, and densities are expressed in units of 10^2 μm^{-3}.

shown in Fig. 16. At variance with the case of oblate, vortex-hosting droplets, where the angular momentum is associated mainly with the vortices, in the case of prolate, vortex-hosting droplets like the one shown in Fig. 16 angular momentum is shared between vortices and capillary waves, the latter being associated with the loss of axial symmetry in the xy plane (in analogy with the case of spinning ^{4}He droplets [38]).

Again, the quasiclassical behavior of the rotating quantum droplets with vortices almost matches that of liquid ^{4}He nanodroplets, as it appears from Fig. 13. Some differences are present though, which are most likely due to finite-size effects and to the small number of vortices. More marked deviations occur, instead, with respect to the universal behavior of incompressible viscous droplets under rotation. The rotational properties of spinning ^{4}He droplets display a clear dependence on the droplet size and the number of vortices they host [38]. In particular, the cusp in the Ω-Λ diagram appears around $\Lambda \simeq 0.7$ (see Fig. 13), at variance with the case of viscous liquid droplets, where the cusp appears at $\Lambda \simeq 1.2$. In general, however, the larger the number of vortices in the droplet, the closer is the behavior of the spinning droplets to the classical ones [38] (that could also be a possible reason of why prolate two-vortex droplets do not follow the common trend of the other cases). We thus expect that bigger quantum droplets with a larger number of vortices in their interior will display a behavior (and cusp position) closer to the classical case. Unfortunately, we were only able to investigate droplets with two or three vortices at most, due to the excessive computational burden discussed before.

IV. CONCLUSIONS

We have studied spinning, self-bound quantum droplets made with the binary Bose mixture ^{41}K - ^{87}Rb. A preliminary analysis of the extended ^{41}K - ^{87}Rb system in the quantum liquid regime shows that the configurations with vortices inside the heavier species, Rb, is the most energetically favored. In the presence of a vortex line in one component alone, the density of the vortex-free species forms an almost empty "fake" core on top of the vortical one. The increased stability with one vortex in the second species is confirmed by studying the rotation of a trapped mixture in the SF regime and subsequent vortex nucleations.

We have then moved to the study of small ^{41}K-^{87}Rb quantum droplets under rotation, focusing on the role of capillary waves and quantized vortices, that are the two main mechanisms with which angular momentum can be stored in spinning superfluid droplets, in determining the rotational properties of QDs.

The resulting (Ω, Λ) phase diagram presents strong similarities, despite the orders-of-magnitude differences in densities and surface tension, with the case of rotating superfluid ^{4}He nanodroplets. In particular, while prolate vortex-free quantum droplets, where angular momentum can only be stored in the form of capillary waves, are on the superfluid branch of the diagram, the vortex-hosting droplets show, instead, a behavior similar to classical rotating liquid droplets, again in analogy with the case of superfluid ^{4}He. The shapes of vortex-hosting droplets can be either axisymmetric (where the angular momentum is stored in the form of singly quantized vortex lines) or prolate (where the angular momentum is shared between vortices and capillary waves). Finite-size effects have been addressed by studying the critical droplet sizes for vortex stability, which are about two orders of magnitude larger than the critical sizes for the stability of vortex-free droplets. Although quantum droplets with such sizes have not been experimentally realized so far for the K-Rb mixture, we believe that this study could be helpful for the interpretation of future experiments aimed at the detection of vortices in quantum droplets, where angular momentum can be deposited in the latter by, e.g., setting into rotation the mixture in the superfluid state and then quenching it into the droplet regime by tuning the interspecies scattering length.

ACKNOWLEDGMENTS

We thank Alessia Burchianti, Manuel Barranco, and Marti Pi for useful comments.

[1] D. S. Petrov, Phys. Rev. Lett. **115**, 155302 (2015).
[2] C. R. Cabrera, L. Tanzi, J. Sanz, B. Naylor, P. Thomas, P. Cheiney, and L. Tarruell, Science **359**, 301 (2018).
[3] G. Semeghini, G. Ferioli, L. Masi, C. Mazzinghi, L. Wolswijk, F. Minardi, M. Modugno, G. Modugno, M. Inguscio, and M. Fattori, Phys. Rev. Lett. **120**, 235301 (2018).
[4] C. D'Errico, A. Burchianti, M. Prevedelli, L. Salasnich, F. Ancilotto, M. Modugno, F. Minardi, and C. Fort, Phys. Rev. Research **1**, 033155 (2019).
[5] Z. Guo, F. Jia, L. Li, Y. Ma, J. M. Hutson, X. Cui, and D. Wang, Phys. Rev. Research **3**, 033247 (2021).
[6] L. Tanzi, E. Lucioni, F. Fama, J. Catani, A. Fioretti, C. Gabbanini, R. N. Bisset, L. Santos, and G. Modugno, Phys. Rev. Lett. **122**, 130405 (2019).
[7] F. Böttcher, M. Wenzel, J.-N. Schmidt, M. Guo, T. Langen, I. Ferrier-Barbut, T. Pfau, R. Bombín, J. Sánchez-Baena, J. Boronat, and F. Mazzanti, Phys. Rev. Research **1**, 033088 (2019).
[8] L. Chomaz, S. Baier, D. Petter, M. J. Mark, F. Wachtler, L. Santos, and F. Ferlaino, Phys. Rev. X **6**, 041039 (2016).
[9] R. N. Bisset, L. A. Pena Ardila, and L. Santos, Phys. Rev. Lett. **126**, 025301 (2021).
[10] C. Fort and M. Modugno, Appl. Sci. **11**, 866 (2021).
[11] V. Cikojević, E. Poli, F. Ancilotto, L. Vranješ-Markić, and J. Boronat, Phys. Rev. A **104**, 033319 (2021).
[12] G. Ferioli, G. Semeghini, L. Masi, G. Giusti, G. Modugno, M. Inguscio, A. Gallemi, A. Recati, and M. Fattori, Phys. Rev. Lett. **122**, 090401 (2019).
[13] V. Cikojević, L. V. Markić, M. Pi, M. Barranco, F. Ancilotto, and J. Boronat, Phys. Rev. Research **3**, 043139 (2021).
[14] R. J. Donnelly, *Quantized Vortices in Helium II* (Cambridge University Press, Cambridge, UK, 1991).
[15] C. F. Barenghi, R. J. Donnelly, and W. F. Vinen, *Quantized Vortex Dynamics and Superfluid Turbulence* (Springer Science and Business Media, Berlin, 2001).
[16] A. L. Fetter, Rev. Mod. Phys. **81**, 647 (2009).
[17] L. Pitaevskii and S. Stringari, *Bose-Einstein Condensation and Superfluidity*, International Series of Monographs on Physics Vol. 164 (Oxford University Press, Oxford, UK, 2016).
[18] B. P. Anderson, J. Low Temp. Phys. **161**, 574 (2010).
[19] A. Cidrim, F. E. A. dos Santos, E. A. L. Henn, and T. Macri, Phys. Rev. A **98**, 023618 (2018).
[20] B. A. Malomed, Phys. D (Amsterdam, Neth.) **399**, 108 (2019).
[21] Y. V. Kartashov, B. A. Malomed, and L. Torner, Phys. Rev. Lett. **122**, 193902 (2019).
[22] Z.-H. Luo, W. Pang, B. Liu, Y.-Y. Li, and B. A. Malomed, Front. Phys. **16**, 32201 (2021).
[23] Y. Li, Z. Chen, Z. Luo, C. Huang, H. Tan, W. Pang, and B. A. Malomed, Phys. Rev. A **98**, 063602 (2018).
[24] P. Examilioti and G. M. Kavoulakis, J. Phys. B **53**, 175301 (2020).
[25] M. N. Tengstrand, P. Stürmer, E. Ö. Karabulut, and S. M. Reimann, Phys. Rev. Lett. **123**, 160405 (2019).
[26] P. Sturmer, M. N. Tengstrand, R. Sachdeva, and S. M. Reimann, Phys. Rev. A **103**, 053302 (2021).
[27] Y. V. Kartashov, B. A. Malomed, and L. Torner, Phys. Rev. Research **2**, 033522 (2020).
[28] S. R. Otajonov, E. N. Tsoy, F. K. Abdullaev, Phys. Rev. E **102**, 062217 (2020).
[29] Y. V. Kartashov, B. A. Malomed, L. Tarruell, and L. Torner, Phys. Rev. A **98**, 013612 (2018).
[30] F. Ancilotto, M. Barranco, M. Guilleumas, and M. Pi, Phys. Rev. A **98**, 053623 (2018).
[31] L. F. Gomez, K. R. Ferguson, J. P. Cryan, C. Bacellar, P. Rico Mayro Tanyag, C. Jones, S. Schorb, D. Anielski, A. Belkacem, C. Bernando, R. Boll, J. Bozek, S. Carron, G. Chen, T. Delmas, L. Englert, S. W. Epp, B. Erk. L. Foucar, R. Hartmann, A. Hexemer *et al.*, Science **345**, 906 (2014).
[32] C. F. Jones, C. Bernando, P. Tanyag Rico Mayro, C. Bacellar, K. R. Ferguson, L. F. Gomez, D. Anielski, A. Belkacem, R. Boll, J. Bozek, S. Carron, J. Cryan, L. Englert, S.W. Epp, B. Erk, L. Foucar, R. Hartmann, D.M. Neumark, D. Rolles, A. Rudenko *et al.*,Phys. Rev. B **93**, 180510(R) (2016).
[33] C. Bernando, P. Mayro R. Tanyag, C. Jones, C. Bacellar, M. Bucher, K. R. Ferguson, D. Rupp, M. P. Ziemkiewicz, L. F. Gomez, A. S. Chatterley, T. Gorkhover, M. Müller, J. Bozek,

S. Carron, J. Kwok, S. L. Butler, T. Möller, C. Bostedt, O. Gessner, and A. F. Vilesov, Phys. Rev. B **95**, 064510 (2017).
[34] D. Rupp, N. Monserud, B. Langbehn, M. Sauppe, J. Zimmermann, Y. Ovcharenko, T. Möller, F. Frassetto, L. Poletto, A. Trabattoni, F. Calegari, M. Nisoli, K. Sander, C. Peltz, M. J. J. Vrakking, T. Fennel, and A. Rouzée, Nat. Commun. **8**, 493 (2017).
[35] B. Langbehn, K. Sander, Y. Ovcharenko, C. Peltz, A. Clark, M. Coreno, R. Cucini, M. Drabbels, P. Finetti, M. Di Fraia, L. Giannessi, C. Grazioli, D. Iablonskyi, A. C. LaForge, T. Nishiyama, V. O. Alvarez de Lara, P. Piseri, O. Plekan, K. Ueda, J. Zimmermann *et al.*, Phys. Rev. Lett. **121**, 255301 (2018).
[36] O. Gessner and A. F. Vilesov, Annu. Rev. Phys. Chem. **70**, 173 (2019).
[37] S. M. O. O'Connell, P. Mayro R. Tanyag, D. Verma, C. Bernando, W. Pang, C. Bacellar, C. A. Saladrigas, J. Mahl, B. W. Toulson, Y. Kumagai, P. Walter, F. Ancilotto, M. Barranco, M. Pi, C. Bostedt, O. Gessner, and A. F. Vilesov, Phys. Rev. Lett. **124**, 215301 (2020).
[38] M. Pi, J. M. Escartin, F. Ancilotto, and M. Barranco, Phys. Rev. B **104**, 094509 (2021).
[39] A. Bohr and B. R. Mottelson, *Nuclear Structure* (W. A. Benjamin, Reading, MA, 1975), Vol. 2.
[40] D. L. Whitaker, M. A. Weilert, C. L. Vicente, H. J. Maris, and G. M. Seidel, J. Low Temp. Phys. **110**, 173 (1998); L. Childress, M. P. Schmidt, A. D. Kashkanova, C. D. Brown, G. I. Harris, A. Aiello, F. Marquardt, and J. G. E. Harris, Phys. Rev. A **96**, 063842 (2017).
[41] R. A. Brown and L. E. Scriven, Proc. R. Soc. London, Ser. A **371**, 331 (1980).
[42] C.-J. Heine, IMA J. Num. Anal. **26**, 723 (2006).
[43] S. L. Butler, M. R. Stauffer, G. Sinha, A. Lilly, and R. J. Spiteri, J. Fluid Mech. **667**, 358 (2011).
[44] K. A. Baldwin, S. L. Butler, and R. J. A. Hill, Sci. Rep. **5**, 7660 (2015).
[45] F. Ancilotto, M. Pi, and M. Barranco, Phys. Rev. B **91**, 100503(R) (2015).
[46] F. Ancilotto, M. Barranco, and M. Pi, Phys. Rev. B **97**, 184515 (2018).
[47] D. V. Osborne, Proc. Phys. Soc. A **63**, 909 (1950).
[48] R. P. Feynman, in *Progress in Low Temperature Physics*, edited by C. J. Gorter (North-Holland, Amsterdam, 1955), Vol. 1, p. 1.
[49] C. D'Errico, M. Zaccanti, M. Fattori, G. Roati, M. Inguscio, G. Modugno, and A. Simoni, New J. Phys. **9**, 223 (2007).
[50] A. Marte, T. Volz, J. Schuster, S. Durr, G. Rempe, E. G. M. van Kempen, and B. J. Verhaar, Phys. Rev. Lett. **89**, 283202 (2002).
[51] F. Minardi, F. Ancilotto, A. Burchianti, C. D'Errico, C. Fort, and M. Modugno, Phys. Rev. A **100**, 063636 (2019).
[52] F. Ancilotto, M. Barranco, F. Coppens, J. Eloranta, N. Halberstadt, A. Hernando, D. Mateo, and M. Pi, Int. Rev. Phys. Chem. **36**, 621 (2017).
[53] J. Garaud, J. Dai, and A. J. Niemi, J. High Energy Phys. 07 (2021) 157.
[54] S. Stringari and J. Treiner, Phys. Rev. B **36**, 8369 (1987).
[55] M. Pi, R. Mayol, A. Hernando, M. Barranco, and F. Ancilotto, J. Chem. Phys. **126**, 244502 (2007).
[56] I. Amelio, D. E. Galli, and L. Reatto, Phys. Rev. Lett. **121**, 015302 (2018).
[57] D. E. Galli, L. Reatto, and M. Rossi, Phys. Rev. B **89**, 224516 (2014).
[58] P. Kuopanportti, S. Bandyopadhyay, A. Roy, and D. Angom, Phys. Rev. A **100**, 033615 (2019); P. Kuopanportti, J. A. M. Huhtamäki, and M. Möttönen, *ibid.* **85**, 043613 (2012).
[59] A. L. Fetter, J. Low Temp. Phys. **16**, 533 (1974).
[60] G. M. Seidel and H. J. Maris, Phys. B: Condens. Matter **194–196**, 577 (1994).